Design and Construction of a Dual Erbium-Potassium Experiment

Lucas Hofer

Christ Church

University of Oxford

A report submitted to transfer to the status of

Doctor of Philosophy

Hilary 2019

Declaration of Authorship

I hereby certify that this report is entirely my own work except where otherwise indicated. Passages and ideas from other sources have been clearly indicated.

Lucas Hofer

Oxford, June 16, 2020

Abstract

This report details my work towards the construction of a dual species erbium-potassium ultracold machine done in the first year of my DPhil. Although I was involved in a number of disparate projects, this report focuses on the experiment's imaging systems, as well as the design and initial construction of the potassium addition. First, an absorption imaging setup was constructed and an image analysis GUI written which allows experimental parameters such as atom number and temperature to be extracted from the images. Second the vacuum, magnetic field and laser systems to create a 2D+ MOT were designed to laser cool either ^{41}K or ^{39}K. The dual-species machine will allow novel impurity physics experiments to be undertaken including the search for exotic Bose polarons and the exploration of non-Markovian quantum information systems—both of which take advantage of the dipole-dipole interactions afforded by the erbium bath.

Contents

1. Introduction

1.1. Overview

The field of atomic, molecular, and optical physics was electrified when the first Bose-Einstein condensates (BEC) were created by Cornell, Wieman [1] and Ketterle [2] in the mid 1990's. A wide array of experiments followed the initial discovery and several groups have spent the last decade studying BECs composed of dipolar gases, which feature a long-range anisotropic dipole-dipole interaction in addition to the more common isotropic contact interactions found in usual BECs. Tilman Pfau's group created the first dipolar BEC composed of chromium (Cr) [3] followed by Benjamin Lev's group's use of dysprosium (Dy) [4] and most recently, an Er BEC created by Francesca Ferlaino's group [5]. Although both Er and Dy offer a significant improvement over Cr, since their larger magnetic moments increase the strength of the dipole-dipole interaction, our group has chosen to work with Er.

The anisotropic nature of the dipole-dipole interaction has led to a number of interesting discoveries [6]. Some of these—such as the roton minimum [7–10] and supersolidity [11–14]—were theoretically anticipated, whereas others, particularly quantum droplets [15–17], were surprising and required theorists to develop new models for their explanation [18]. A number of dipolar quantum gas experiments exist around the world or are currently under construction. However, the erbium experiment at Oxford differs from these in two key ways. First, rather than the atoms being placed in a harmonic trap as in most atomic physics experiments, a homogeneous box trap will be used [19, 20] which should prove advantageous when studying density dependent phenomena such as Kibble-Zurek scaling in quantum phase transitions [21]. The other difference is that a second atomic species, potassium, will be added to the experiment which will allow other interesting phenomena such as impurity physics with exotic polarons [22,23] and non-Markovian systems [24, 25] to be studied with a high degree of tunability.

Isotope	^{162}Er	^{164}Er	^{166}Er	^{167}Er	^{168}Er	^{170}Er
Abundance (%)	0.14	1.61	33.6	23.0	26.8	15.0

TABLE 1.1.: Relative natural abundance of the various erbium isotopes (adapted from [27]).
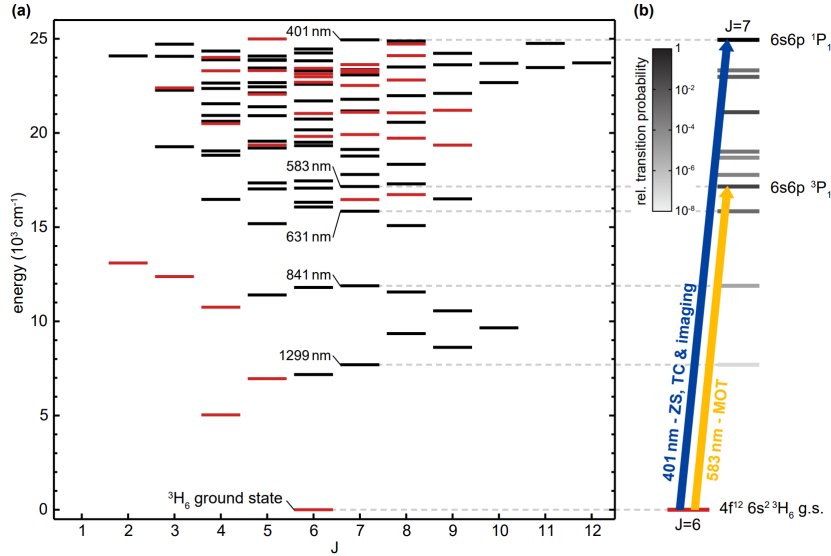

FIGURE 1.1.: (a) Energy level diagram of erbium. (b) The two transitions used for laser cooling erbium. Image taken from [28]

1.2. Erbium

Erbium is a lanthanide with a submerged shell in the following configuration $(1s^2 2s^2 2p^6 3s^2 3p^6 4s^2 3d^{10} 4p^6 5s^2 4d^{10} 5p^6) 6s^2 4f^{12}$ which gives a magnetic moment of $7\ \mu_B$. Since the isotopes ^{166}Er and ^{168}Er—which are used in the experiment (see Table 1.1)—have no nuclear spin, there is no hyperfine structure. This, in addition to more complex mechanisms [26], significantly simplifies the cooling scheme with no repump lasers required. A 401 nm transition is used for initial cooling in the Zeeman slower, whereas a narrower 583 nm transition is used for cooling in the 3D MOT (see Fig. 1.1).

1.3. Potassium

Potassium is an alkali atom with an electronic configuration of $1s^2 2s^2 2p^6 3s^2 3p^6 4s^1$. It has two stable bosonic isotopes ^{39}K and ^{41}K along with an effectively stable fermionic isotope ^{40}K (see Table 1.2) all of which have been successfully cooled to

Isotope	^{39}K	^{40}K	^{41}K
Abundance (%)	93.258	0.012	6.730

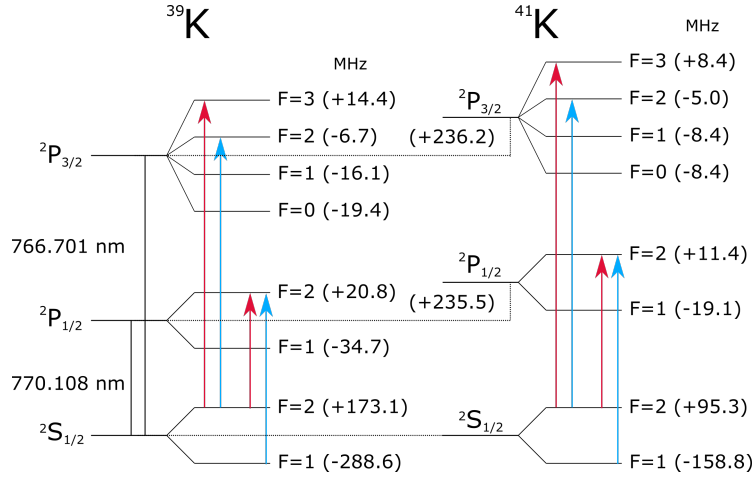TABLE 1.2.: Relative natural abundance of the various stable potassium isotopes.

FIGURE 1.2.: Energy level scheme for laser cooling ^{39}K and ^{41}K. For both isotopes the D2 transition $^2S_{1/2}$ to $^2P_{3/2}$ is used for initial cooling and the compressed MOT, whereas the D1 transition $^2S_{1/2}$ to $^2P_{1/2}$ is used for the compressed MOT and the grey molasses cooling. The red arrow denotes the cooling line in each of the respective transitions, whereas the blue arrow represents the repump laser used to achieve closed optical cycling.

quantum degeneracy. Our potassium setup has been designed to cool either ^{39}K or ^{41}K, but will focus initially on ^{41}K due to its favourable scattering properties at low magnetic fields. Although potassium was originally brought to quantum degeneracy via sympathetic cooling, a compressed MOT in conjunction with a grey molasses cooling stage has successfully created BECs for both ^{39}K [29] and ^{41}K [30]. This involves using the D2 transition at 767 nm ($^2S_{1/2}$ state to the $^2P_{3/2}$) for initial cooling and the compressed MOT, whereas the D1 transition at 770 nm ($^2S_{1/2}$ state to the $^2P_{1/2}$) is also used for the compressed MOT and then alone for the grey molasses. Both the D2 and D1 transitions need a cooling and repump laser to achieve closed optical cycling due to the hyperfine structure (see Fig 1.2).

1.4. Report Overview

This report focuses both on the additions that have been made to the main erbium experiment (see Fig. 1.3) over the past year as well as the design of the potassium system. In particular, the second chapter details the absorption imaging setup as
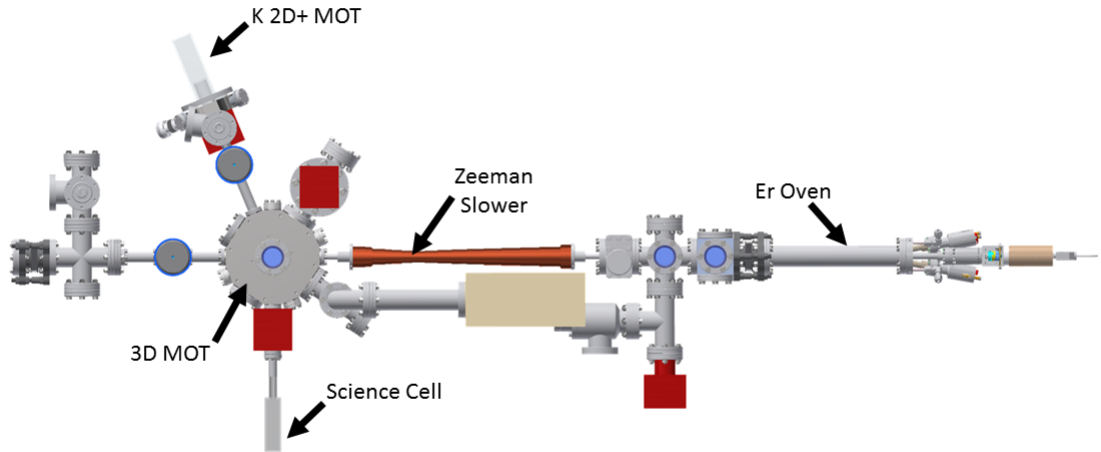
Figure 1.3.: The vacuum setup for cooling erbium and potassium. The oven containing erbium, in conjunction with an aperture, creates an atomic beam with a velocity peaked at 500-600 m/s. The beam passes through the Zeeman slower where a counter propagating beam of 401 nm light slows the atoms longitudinally in conjunction with the Zeeman slower's magnetic field. The slowed atoms then pass into the 3D MOT chamber where a six beam configuration of 583 nm lasers (each roughly 30 mm in diameter) and quadrupole magnetic field further cool and trap the atoms. For the potassium atoms, a 2D+ MOT creates a slow beam of atoms which pass into the 3D MOT chamber and are similarly cooled and trapped by a six beam configuration.

well as the imaging software used for experimental image analysis. Chapter three describes the design and initial construction of the potassium addition. Future impurity physics experiments are then detailed in the fourth chapter. Lastly, a series of appendices address the sizeable number of more technical projects that were accomplished throughout the course of the year including a MySQL database for recording experimental data, a camera control program, a data analysis GUI and lastly an object detection neural network which is used to automatically find atomic clouds in images.

2. Absorption Imaging

2.1. Introduction

Absorption imaging is a method used in cold atomic physics to probe an atomic cloud as it yields spatial information that can be used to determine atom number and temperature. A resonant laser beam is shone onto the atoms creating a "shadow" in the beam which is imaged then to determine the atom density. A probe beam passing through a cloud of atoms is attenuated by

$$I(\omega, x, y) = I_0 e^{-OD(\omega, x, y)} \tag{2.1}$$

where I_0 is the initial intensity of the beam. OD is the optical depth given by

$$OD(\omega, x, y) = \int \sigma(\omega) n(x, y, z) dz. \tag{2.2}$$

where σ is the optical cross section and n is the atomic density. During absorption imaging, the probe laser frequency is set to resonance at $\omega = \omega_0$.

The MOT in the erbium experiment uses the narrow-line 583 nm transition and is thus intrinsically spin-polarized [31] since the atoms primarily scatter off the bottom σ- beam which transfers atoms to the lowest spin state i.e. $m_J = -6$. During the absorption imaging pulse, σ- light drives the transition from the ground $m_J = -6$ to the excited state $m'_J = -7$ and is effectively a two-level system. The optical cross section $\sigma(\omega)$ can then be given by

$$\sigma = \left(\frac{3\lambda^2}{2\pi} \right) \frac{1}{1 + 4 \left(\frac{\Delta}{\Gamma} \right)^2 + \frac{I_0}{I_{\text{sat}}}} \tag{2.3}$$

where λ is the wavelength of the transition, Δ is the detuning, Γ is the natural line width, I_0 is the intensity of the probe beam and I_{sat} is the saturation intensity (60 mW/cm^2 for erbium's 401 nm transition and 1.75 mW/cm^2 for potassium's D2 transition). When driving the transition resonantly, $\Delta = 0$ and when $I_0 \ll I_{\text{sat}}$ this gives
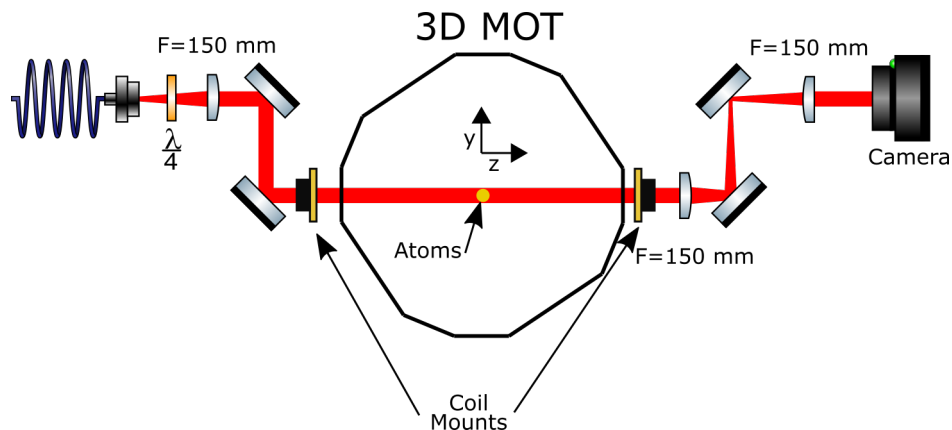
$$\sigma_0 \approx \frac{3\lambda^2}{2\pi}. \tag{2.4}$$

FIGURE 2.1.: Resonant light exits the fibre and passes through the $\lambda/4$ plate where the σ-polarization is set. The beam is then collimated with the 150 mm lens and passes into the MOT chamber and through the atomic cloud. Upon exiting the chamber, the atom image is collimated first with the 150 mm lens and then either magnified or demagnified by a second lens before being imaged with the camera sensor. The two coils in a quasi-Helmholtz configuration create a quantization axis along the z-axis for imaging the atoms.

The 401 nm transition is used for imaging as it has a higher saturation intensity and thus higher intensities can be used while staying in the $I_0 \ll I_{\mathrm{sat}}$ regime—providing a better signal to noise ratio.

2.2. Experimental Setup

The 3D MOT chamber has two ports for absorption imaging—one for entry and one for exit of the beam (see Fig. 2.1). In addition to the optics, magnetic fields are needed to create a quantization axis along the beam's axis of propagation.

2.2.1. Optics

The optics consist of a two separate cage systems (see Fig. 2.2). The first cage system collimates a probe beam of 401 nm light to a diameter of 23.3 mm and sets the polarization to σ- with a $\lambda/4$ wave plate. This light then passes through the MOT chamber and the atoms (see Fig. 2.1) after which the beam enters the second cage system which uses a series of lenses to either magnify or demagnify the atom image before it is incident on a camera.
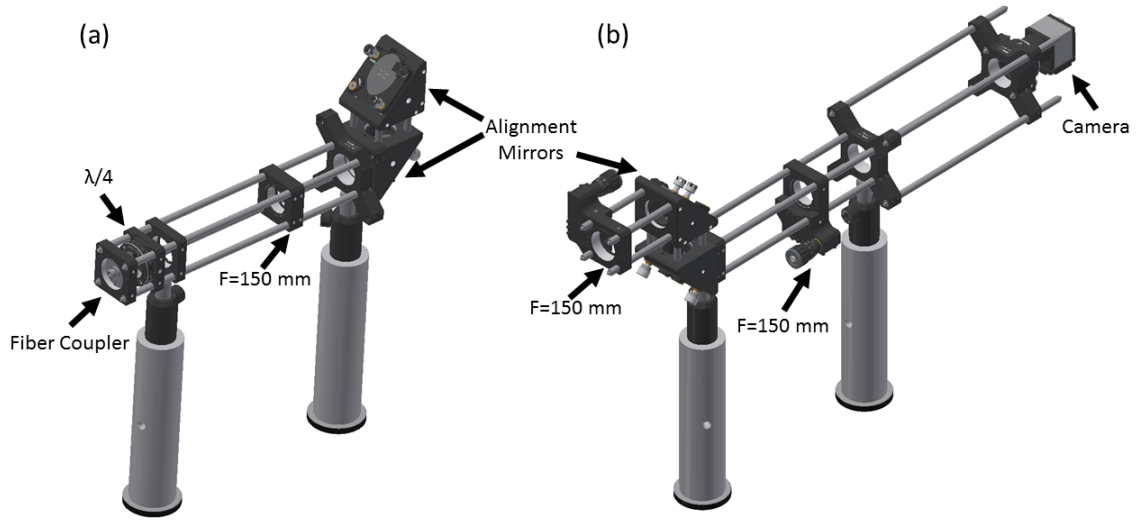
FIGURE 2.2.: (a) Cage system for the probe beam side optics. (b) Cage system for the camera side optics.

2.2.2. Magnetic Fields

A set of quasi-Helmholtz coils creates the requisite magnetic fields for absorption imaging. Due to the tight geometry surrounding the view ports on the 3D MOT, the coils could not be placed equidistant from the centre of the MOT chambers. As such, the number of windings per coil needed to be carefully calculated such that the magnetic field of 2 G was uniform at the MOT centre (see Fig. 2.3). The coil on the input side (see Fig. 2.4a) was placed 158 mm away from the centre and has 57 windings, whereas the coil on the camera side (see Fig. 2.4b) was placed 133 mm from the centre of the chamber with 28 windings. Both coils use 1 mm diameter copper wire and have an inner radius of 30 mm. The coil mounts were custom designed and printed on an Ultimaker 3 3D printer with CPE+ material.

2.3. Imaging Sequence

During an experimental sequence three images are needed. First, the probe beam is shone through the atoms in a short pulse (15 μs). This gives the information about the atom cloud (I_a) and simultaneously blows away all the atoms. Next, an image is taken of the probe beam without the atoms (I_p). Lastly, an image is taken
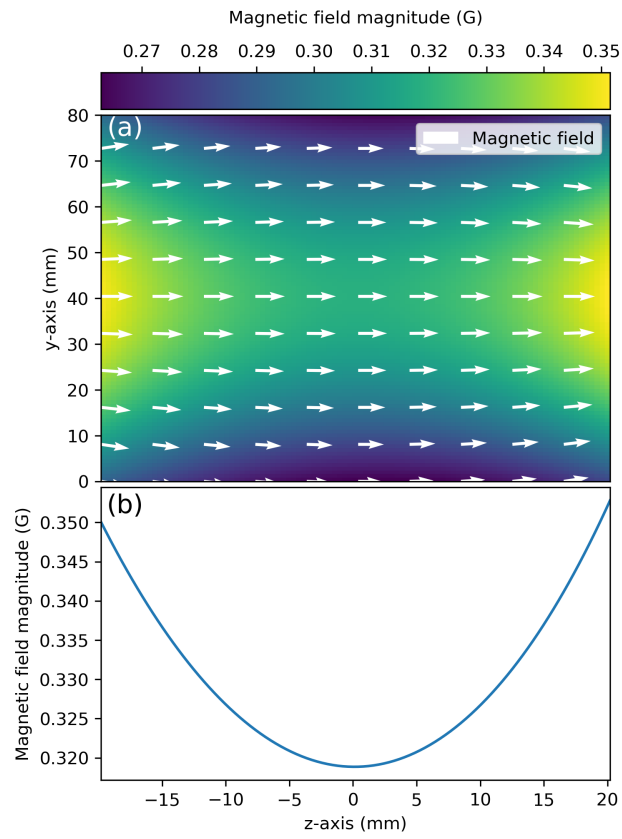
FIGURE 2.3.: (a) Magnetic field magnitude in the YZ plane at $x=0$. The field is aligned along the z axis (imaging axis) providing the necessary quantization axis for the atoms. (b) The magnetic field magnitude along the z axis. The centre of the quasi-Helmholtz magnetic field configuration is clearly located at the centre of the MOT. The magnetic field for both (a) and (b) is given for 1 A of current.

FIGURE 2.4.: (A) Coil mount for the probe beam side of the MOT chamber. (B) Coil mount for the camera side of the MOT chamber.

without atoms or the probe beam (I_b). Optical density is then calculated as

$$OD = \log\left(\frac{I_p - I_b}{I_a - I_b}\right) \tag{2.5}$$

from which the cloud can be fitted and information such as atom number and temperature can be extracted.

2.4. Image Analysis

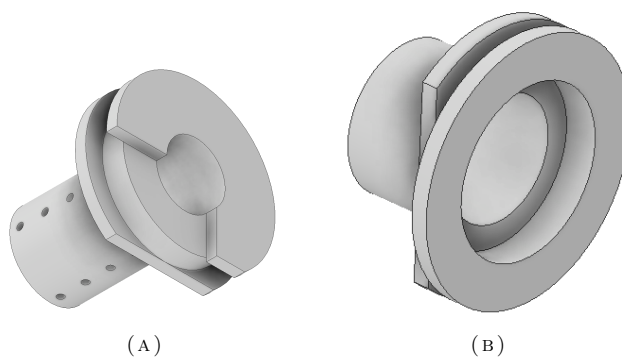The primary data recorded from the experiments are images (see Appendix A). Although images can be analysed in simple Python or Matlab scripts, a custom analysis GUI (see Fig. 2.5) has been written (see Appendix B) which allows the user to pull images and the experimental control data associated with the images (such as coil currents, detunings and hold times) from the file system and database for analysis. The images can be analysed with tools such as area of interest selection and 2D Gaussian fits.

2.4.1. Object Detection Neural Network

The analysis GUI is able to automatically determine where an atomic cloud is located. When looking at time of flight (TOF) images (see Fig. 2.6) this is particularly useful as the atoms fall during the course of the measurement and thus necessitate a unique area of interest per image which is tedious to manually determine. Therefore, a neural network approach was utilized to determine the location of the cloud (see Appendix C). Although other methods can be used to determine the location of the cloud, these methods have more difficulty adapting to diverse environmental conditions than an optimized neural network.

2.4.2. Atom Number

The absorption imaging setup has been put in place and is currently used for primary data acquisition (see Fig 2.7). A fit of the optical depth (when the transition is unsaturated) can be used to determine the atom number N with the following equation

$$N = \frac{2\pi OD_{\mathrm{pk}}\sigma_x\sigma_y}{\sigma_0} \tag{2.6}$$

where OD_{pk} is the peak optical depth, σ_x is the standard deviation along the x-axis and σ_y is the standard deviation along y-axis. All of these values are determined
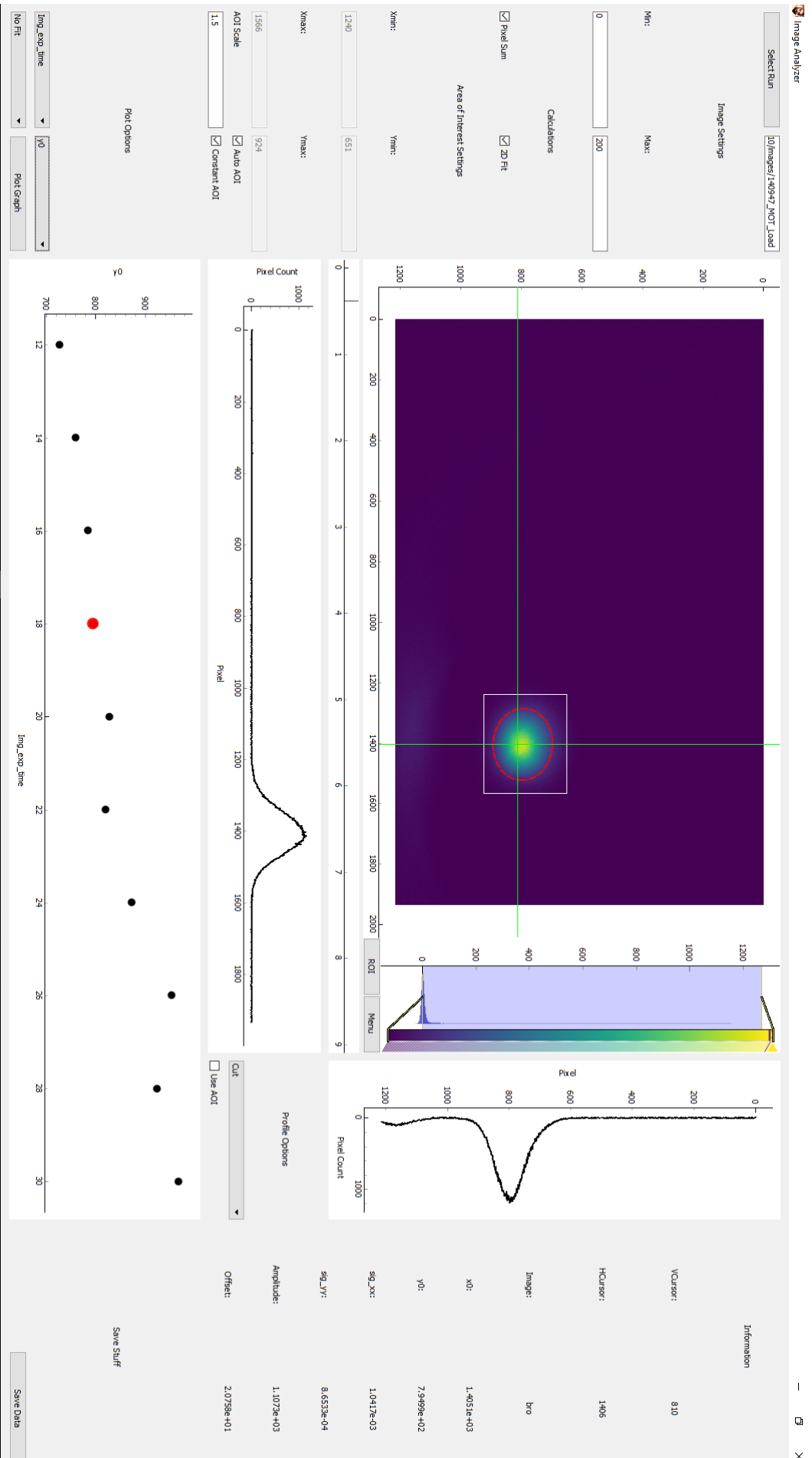
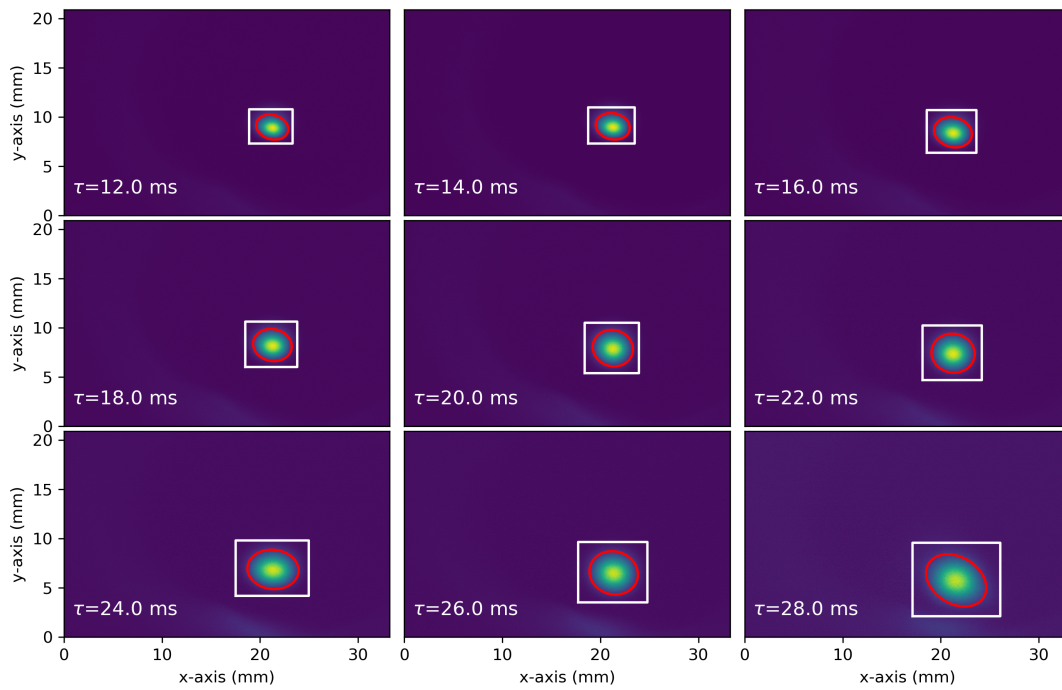Figure 2.5.: The data analysis GUI.

FIGURE 2.6.: Time of flight data in which an atomic cloud is released from a compressed MOT. The time after release is given by τ (ms) and the object detection neural network determines the area of interest (white box) within which the 2D Gaussian is fit and the fitting parameters used to calculate the temperature (see Fig. 2.8).
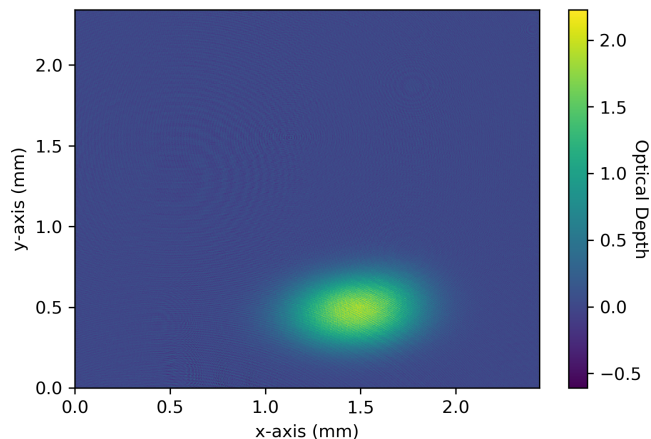
Figure 2.7.: Absorption image of the compressed MOT.

from a 2D Gaussian fit. Lastly, σ_0 is the optical cross-section at resonance. We find that in a scan of the MOT frequency detuning the absorption measurement returns a maximum atom number of 7.6×10^7 atoms (see Fig. 2.7).

2.4.3. Temperature Measurements

The temperature of the atomic cloud is an important measurement to make as it helps determine whether a significant number of atoms can be further loaded into an optical dipole trap. The temperature can be extracted from a time of flight measurement in which the atoms are released from the trap and allowed to both freely expand and fall under gravity. An area of interest for the cloud is determined, the atomic cloud fit with a 2D Gaussian and the fitted cloud widths used to extract the temperature (see Fig. 2.8) using

$$\sigma^2 = \sigma_{\text{trap}}^2 + \frac{k_B T \tau^2}{m}. \tag{2.7}$$

where σ_{trap} is the initial trap size, k_B is Boltzmann's constant, m is the mass of the atomic species, T is the temperature in Kelvin and τ is the time since the cloud was released from the trap.
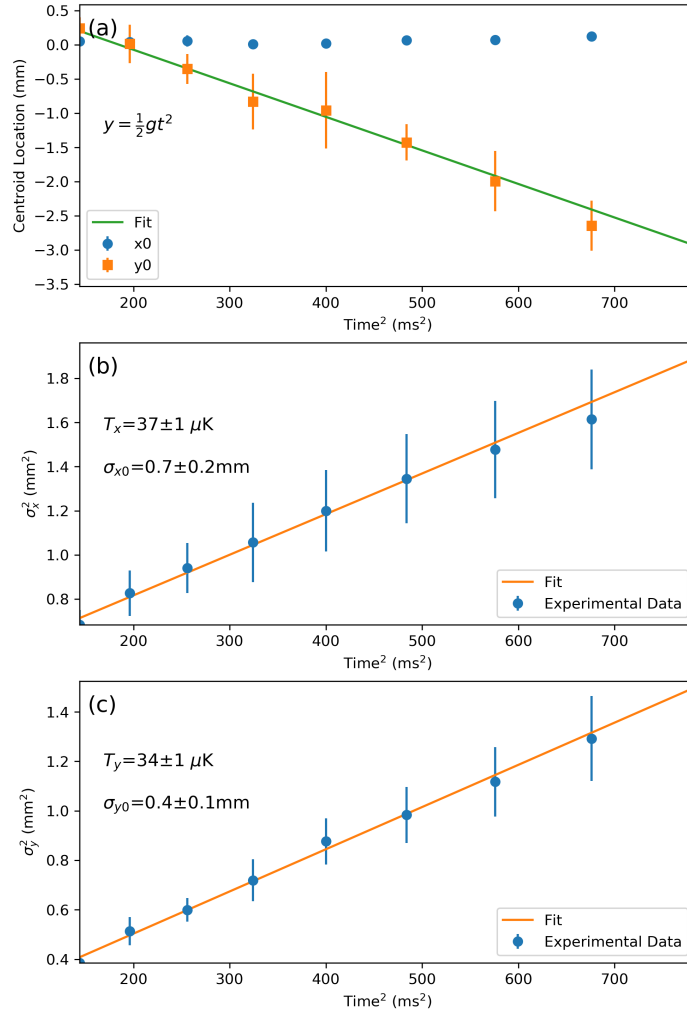
FIGURE 2.8.: (a) Centroid location as a function of time since the cloud was released from the trap for both the x (circles) and y (squares) axes which were found from the fits in Fig. 2.6. Note that the cloud drops after released due to gravity and is used to calibrate the magnification of the system such that the slope of the line is $\frac{1}{2}g$ where g is the gravitational constant. (b) The size of the cloud along the x axis as a function of time since release squared. Using Eq. 2.7 the temperature T_x and cloud size in the trap σ_{x0} can be determined. (c) The size of the cloud along the y axis.

3. Potassium Addition

3.1. Potassium

In order to perform impurity experiments, a second atomic species is being added to the current erbium machine. However, this second atomic species must be cooled without a Zeeman slower due to limited space on the experiment table and additionally must have favourable scattering properties i.e. a multitude of inter-species Feshbach resonances. We choose potassium as it can be cooled from a background vapour using a 2D magneto-optical trap (MOT) and has a rich Feshbach resonance spectrum which should lead to a similarly dense spectrum for the inter-species mixture.

3.2. Overview

The potassium setup begins with a 2D+ MOT which creates a slow atomic beam from a background vapour. This atomic beam then enters the 3D MOT chamber where it will be trapped and cooled to quantum degeneracy. In the past, sympathetic cooling was necessary, but recent experiments have achieved degeneracy by using a grey molasses cooling stage [29, 30]—which we plan to do with our setup.

3.3. 2D+ MOT

In the 2D+ MOT a heated background vapour of potassium is trapped along only two dimensions which creates a line of atoms trapped along the z-axis of the chamber (see Fig. 3.1). These atoms are then pushed into the 3D MOT chamber via another laser beam to create an atomic beam with a high flux. The 2D+ MOT required several custom components to be designed such as a coil arrangements for the MOT's quadrupole magnetic field, an oven to keep the potassium atoms hot (40-50°C) and an optics setup to create the large laser beams for trapping.
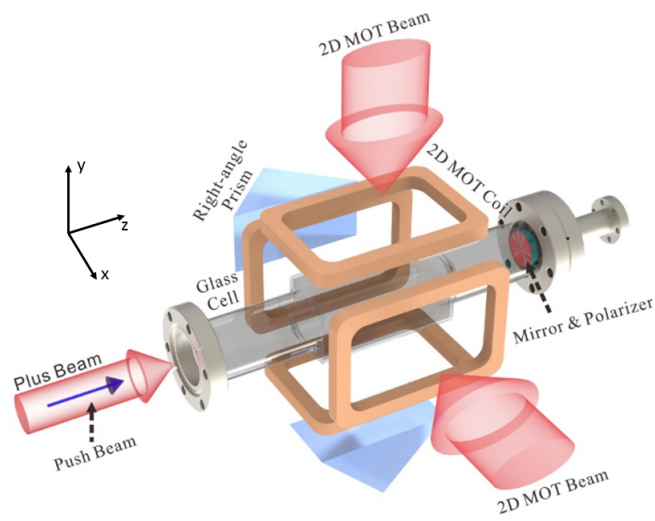
FIGURE 3.1.: Example of 2D+ MOT taken from [30]. The atoms are contained inside the glass cell which has two pairs of anti-Helmholtz coils around it to create a quadrupole field. Two elliptical beams shine into the cell and are retro-reflected (our setup will have four independent beams) to trap a line of atoms. A molasses beam enters from the back of the cell (plus beam) and is retro-reflected by the polariser and mirror combination which allows the relative intensity of the incoming and outgoing beam to be adjusted. Lastly, a blue detuned beam (push beam) pushes the atoms out of the 2D MOT and creates the slow atomic beam.
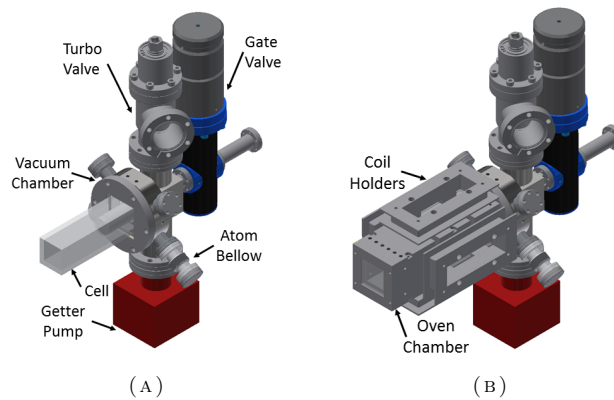
FIGURE 3.2.: (A) Vacuum setup for the 2D+ MOT. Both the oven and the magnetic coils have been removed for clarity. (B) With oven and magnetic field coils.

3.3.1. Main Chamber

The 2D+ MOT is comprised of a glass cell surrounded by two sets of anti-Helmholtz coils orthogonal to one another. These coils create a quadrupole magnetic field necessary for trapping atoms along the x and y axes, but leave a null field along the z axis. A single, red-detuned, circularly polarised laser beam passes through the centre of each coil which, along with the quadrupole magnetic field, creates a harmonic trapping potential along the x and y axes and thus a small cloud of atoms elongated along the z axis (as it has no trapping potential). A fifth red-detuned beam propagates along the z axis from the back of the cell and is reflected by a polariser and mirror at the front of the cell. This creates a molasses along the z axis which further slows the atoms and increases the total flux of the resulting atomic beam. Lastly, a small blue detuned beam propagates along the z axis and pushes the atoms out of the 2D MOT through a small hole in the mirror—thus creating an atomic beam.

3.3.2. Vacuum Design

Custom Vacuum Chamber

A gate valve connects the main experiment's vacuum system to the potassium setup's vacuum system (see Fig. 3.2a). The potassium vacuum system begins with a custom vacuum chamber made of stainless steel. The chamber includes several key components. First, the chamber has two CF40 flanges which connect to a SAES Getter pump and an angle valve (to connect a turbo pump to pump down the chamber). Second, the chamber has a differential pumping tube, which in

conjunction with the getter pump will maintain the pressure gradient between the 2D MOT and the 3D MOT chamber. Lastly the vacuum chamber has a large flat surface with a groove for an indium wire. The glass cell will press against this surface and the vacuum will be sealed with the indium. Potassium is highly reactive with other metals (e.g. stainless steel) which can cause vacuum leaks at glass-to-metal seals. Therefore, indium is used at the glass-to-metal seal which—from discussions with other groups—eliminates vacuum leaks due to potassium [32].

Atom Source

The potassium atoms are sourced from a 5 gram ampoule which will be placed in a bellow attached to the the main vacuum chamber. The bellow allows the ampoule to be broken once the vacuum system is pumped down. A heater will be placed around the bellow to heat the atoms to the requisite 80-100 °C.

Glass Cell

Due to spatial constraints we needed a custom cell measuring 40x40x140 mm. Additionally, the cell has a glass flange 10 mm thick with an 80 mm outer diameter which is used for connection with the custom vacuum chamber. The cell is AR coated at 767-770 nm to reduce back reflections.

Pressure Differential

The background vapour pressure for potassium is $\sim 10^{-7}$ mbar at 40-50 °C but the pressure required in the experimental chamber is on the order of 10^{-12} mbar. Differential pumping is employed to maintain this pressure differential by using a 105 mm tube with a 2 mm diameter in the 2D MOT which gradually increases to a 5 mm diameter in the custom vacuum piece. A layout of the overall vacuum system can be seen in Fig. 3.3a. The pressures and conductances in a vacuum system can be calculated analogous to a electronic circuit (see Fig. 3.3b) with the pressure equal to voltage and the resistance given by $R = \frac{1}{C}$, where C is the conductance between two different elements. Vacuum pumps can be modelled as a conductance S followed by a sink to ground, whereas the 2D MOT with its ampoule of potassium acts as a voltage source. The analogous electronic circuit was solved using Mathematica for our system yielding a pressure of 6×10^{-12} mbar in the MOT chamber and 6×10^{-13} mbar in the science chamber. The ability to maintain the large pressure difference between the 2D MOT and 3D MOT is primarily due to the narrow tube between the 2D MOT and the custom vacuum piece which has

(A)

(B)
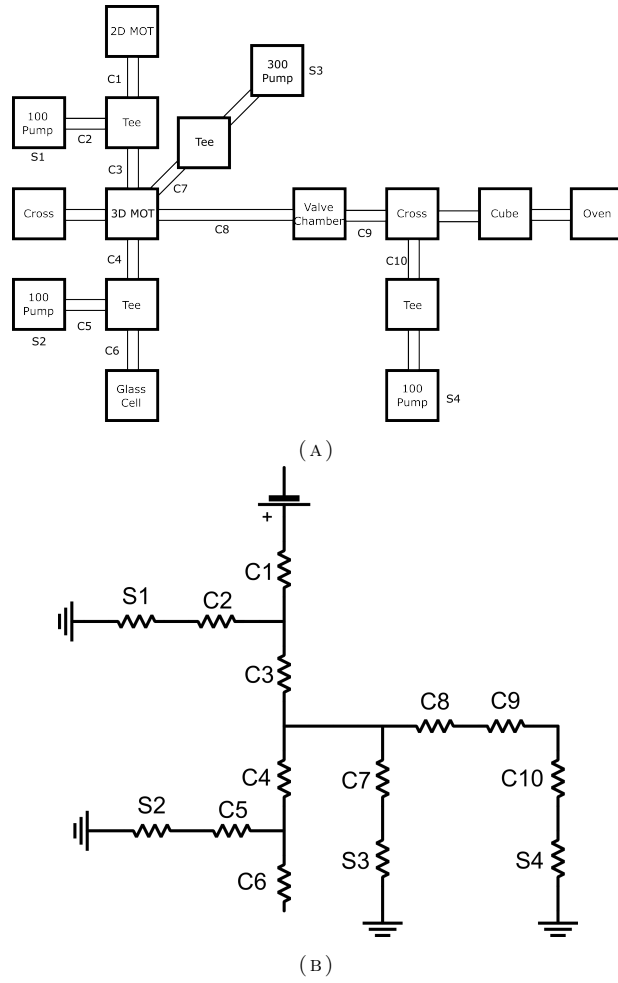
FIGURE 3.3.: (a) Diagram of the overall vacuum system. (b) Analogous electronic circuit used for calculating pressures.

a conductance of 0.02 L/s and the 100 L/s Getter pump attached to the custom vacuum piece.

3.3.3. Oven

An oven is placed around the glass cell to keep the atoms from cooling and sticking to the edge of the cell (see Fig. 3.2b). The oven is designed to be free-standing—so as not to touch the cell—with a light seal created by pressing up against the glass cell holder to keep the hot air inside. The oven will have five windows which are AR coated at 767-770 nm for optical access for the trapping and push beams. Additionally, the four coil mounts (for generating the magnetic fields) are attached

	Min Lit δ/Γ	Min Exp δ/Γ	Max Lit δ/Γ	Max Exp δ/Γ
D2 Cool	-8.9	-10.0	-3.6	-1.7
D2 Repump	-8.4	-14.3	-1.5	2.4
D1 Cool	0.0	-0.4	5.5	8.0
D1 Repump	0.0	-6.9	5.5	9.8
Push/Img Cool	0.0	-5.8	3.0	10.8
Push/Img Repump	0.0	-5.9	3.0	10.7

TABLE 3.1.: Both literature and our experimental detunings for ^{41}K [30,33] given in terms of Γ where $\Gamma/2\pi = 6.035$ MHz [34].

	Min Lit δ/Γ	Min Exp δ/Γ	Max Lit δ/Γ	Max Exp δ/Γ
D2 Cool	-8.9	-9.8	-3.0	-1.8
D2 Repump	-8.4	-9.9	-3.0	-1.9
D1 Cool	0.0	0.5	5.3	8.5
D1 Repump	-0.0	-3.2	5.3	4.8
Push/Img Cool	0.0	-5.8	3.0	10.8
Push/Img Repump	0.0	-5.9	3.0	10.7

TABLE 3.2.: Both literature and our experimental detunings for ^{39}K [30,33] given in terms of Γ where $\Gamma/2\pi = 6.035$ MHz [34].

to the outside of the oven.

3.3.4. Magnetic Field

The magnetic field generated by the two sets of anti-Helmholtz coils is quadrapole along the x and y axes and null along the z axis. A Python program was written to simulate the magnetic field (see Fig. 3.4) and it was determined that each rectangular coil needed 99 turns with an inner length of 12.5 cm and an inner width 5 cm to achieve a magnetic field gradient up to 9-13 G/cm (based on previous literature [30]).

3.4. Laser Systems

The general cooling schematic for ^{41}K and ^{39}K was given in Fig. 1.2 and from previous experiments we determine the range of frequencies needed for both the 2D+ and 3D MOT (see Table 3.1 and Table 3.2). We then designed an optical setup which can cool both ^{41}K and ^{39}K and has a high degree of both frequency and intensity tunability.
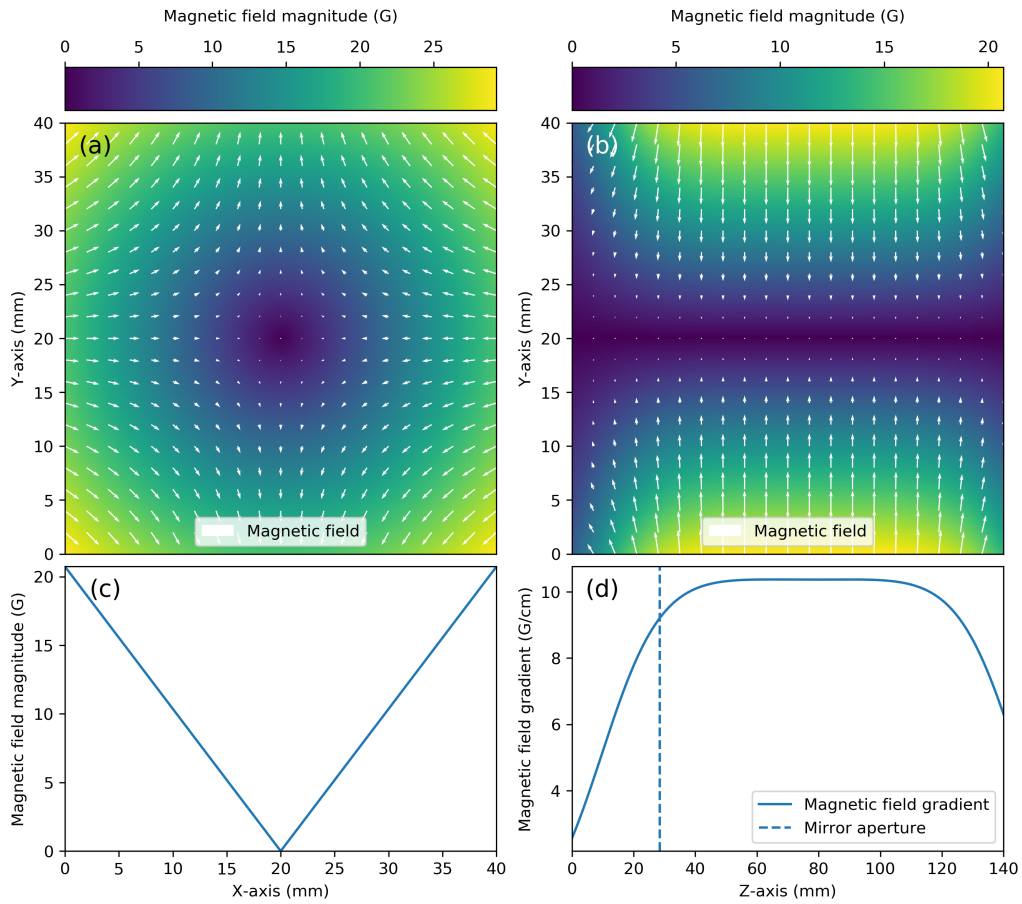
FIGURE 3.4.: (a) The magnitude of the magnetic field in Gauss with the cut orthogonal to the z axis. Note the quadrupole field. (b) The magnitude of the magnetic field with the cut now orthogonal to the x axis. Along the centre of the trap the magnetic is both null and homogeneous. Due to the symmetry of the coils, the cut orthogonal to the y-axis is identical. (c) The magnetic field magnitude vs. the x axis at the centre of the trap. Note the linear slope which is used to calculate the magnetic field gradient. (d) The magnetic field gradient (MFG) along the z axis in G/cm (solid line). The MFG increases rapidly and in the centre of the coils plateaus to a constant values of approximately 10 G/cm. The position of the mirror aperture is denoted with the dotted line.

Figure 3.5.: Optical setup for producing the required frequencies and power for cooling either
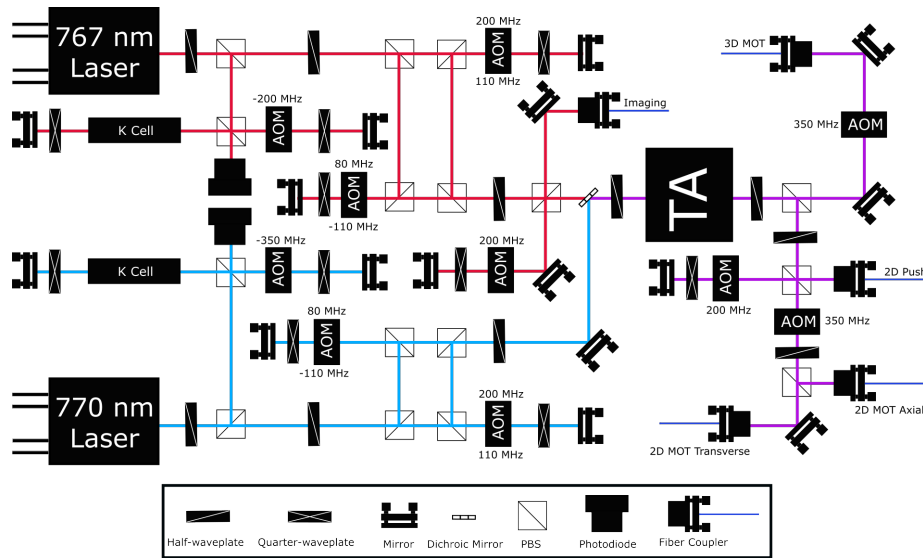^{41}K or ^{39}K. For AOMs with two frequency labels, the top label denotes the AOM frequency used
for cooling ^{41}K, whereas the bottom label gives the AOM frequency used for cooling ^{39}K.

3.4.1. Optics Table

Although previous groups utilized EOMs [35] or a large number of tapered amplifiers
(TA) [30, 36], our setup uses only two seed lasers, one tapered amplifier and a
number of AOMs (see Fig. 3.5)—which allows for a greater degree of tunability
over the cooler and repumper detunings.

Locking

The D2 and D1 lines each have their own seed laser in addition to a heated
potassium vapour cell for locking via saturated absorption spectroscopy. The D1
laser is locked to the ^{39}K F=1 to F'=2 transition (see Fig. 3.6a), whereas the D2
laser is locked to the ^{39}K crossover (see Fig. 3.6b). A double-pass AOM before each
of the spectroscopy cells allows for an overall frequency shift to be applied to each
seed laser and can therefore be used to switch between ^{41}K and ^{39}K—which have a
rough frequency offset of 235 MHz.

Cooling Light

The cooler and repumper light (frequency-tuned with a series of AOMs) from the
D2 and D1 lines is combined on a dichroic mirror before passing through a TA for
amplification. The TA can output roughly 3W of power which is sufficient for both
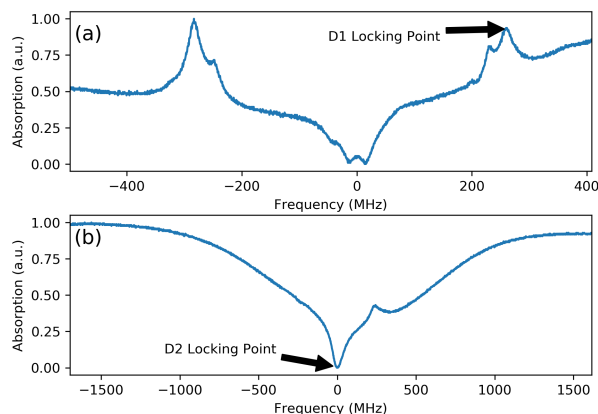
FIGURE 3.6.: (a) Absorption as a function of frequency for the ^{39}K D1 transition with locking point denoted. (b) Absorption as a function of frequency for ^{39}K D2 transition.

the 2D and 3D MOT. After amplification, the light is split into three branches: one for the 2D MOT trapping beams, one for the 2D MOT push beam and one for the 3D MOT beams. For both MOT branches, the light passes through a single pass AOM before being fibre-coupled—which allows for the intensity to be rapidly changed during experimental sequences. The branch with the push beam has a double-pass AOM to allow the frequency and intensity to be tuned.

3.4.2. 2D MOT Optics

Although the power and frequencies are set by the optics on the optics table, the beams need final shaping before passing into the MOT. Instead of buying or building a fibre-coupling array, two spliceless arrays—one with four outputs for the 2D MOT and a second with six output for the 3D MOT—were purchased. Each of the four transverse beams must be elliptical (roughly 75 mm x 25 mm) with a circular polarisation. The axial beam must be circular and contain both the blue detuned push beam at approximately 2 mm diameter (to match the hole in the polariser/mirror) and the red detuned molasses beam at a 25 mm diameter. Additionally, this beam must have the polarisation set correctly to work with the polariser on the mirror inside the cell. An optics schematic for both the transverse beams and axial beam can be seen in Fig. 3.7.
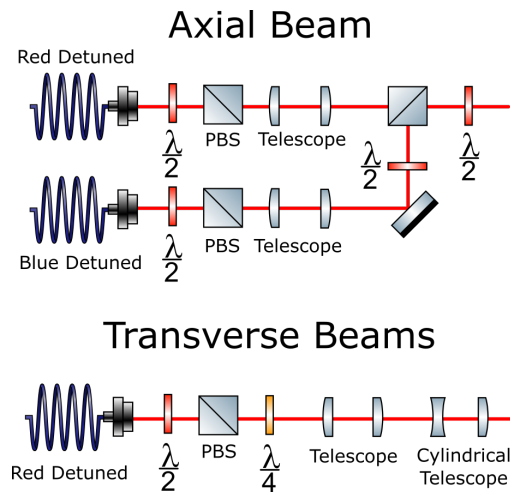
Axial Beam

Red Detuned

$\frac{\lambda}{2}$ PBS   Telescope $\frac{\lambda}{2}$ $\frac{\lambda}{2}$

Blue Detuned $\frac{\lambda}{2}$ PBS   Telescope

Transverse Beams

Red Detuned $\frac{\lambda}{2}$ PBS $\frac{\lambda}{4}$ Telescope   Cylindrical Telescope

FIGURE 3.7.: Optics surrounding the 2D MOT for both the transverse and axial beams.

3.5. Construction

Currently, most of the vacuum parts have been ordered and delivered including the custom vacuum chamber, glass cell, valves, bellows and getter pump. Only a few support pieces and the metal piece which holds the glass cell in place must be completed by the workshop. During a lull in the main experiment's progress the vacuum systems will be installed.

Concurrent to the main experiment, the optical systems for the potassium setup are currently being constructed. Both the seed lasers and tapered amplifier have already been purchased and placed on the optical table. Additionally, all the necessary AOMs have been ordered for cooling ^{41}K—along with most of the optics including beam splitters, waveplates, vapour cells, mirrors and mounts. Lastly, initial testing of the locking scheme has already been completed (see Fig. 3.6)

4. Proposed Er-K Experiments

As of this report's submission, the erbium experiment is moving towards Bose-Einstein condensation while work is also being completed on the potassium addition. Upon completion, two experiments are proposed for the dual erbium-potassium machine, both of which involve the potassium atom acting as an impurity in an erbium bath.

4.1. Experimental Procedure

Additional experimental considerations must be taken into account when loading two atomic species into the same trap. In the dual-species machine we plan to first load the potassium atoms into 3D MOT and then the optical dipole trap. Subsequently the erbium MOT will be loaded and the erbium atoms added to the optical dipole trap. While loading the erbium MOT, the erbium atoms will sit below the optical dipole trap (already loaded with potassium) due to gravitational sag. The potassium atoms are loaded first since the potassium's compressed MOT stage requires much higher magnetic field gradients than erbium—which would cause losses in the erbium atoms if they were loaded into the optical dipole trap first. Although fermi-fermi mixtures require the dipolar species to sympathetically cool the non-dipolar species [37], in our bose-bose mixture each species can be evaporatively cooled on its own or the erbium atoms could be used to sympathetically cool the potassium atoms—the best method will need to be experimentally determined.

4.2. Bose Polarons

The first type of impurity experiment to be undertaken is looking for exotic types of polarons. A polaron is a quasi-particle that is formed when an electron moves through a lattice of atoms (see Fig. 4.1). The atoms in the lattice are attracted to the electron thereby creating elementary excitations termed polarons [38]. Instead of an electron, this system will be simulated with potassium atoms in a BEC of erbium atoms. The impurity atoms are dressed by the excitations (phonon excitation spectrum in a normal BEC) of the surrounding bath leading to a Bose
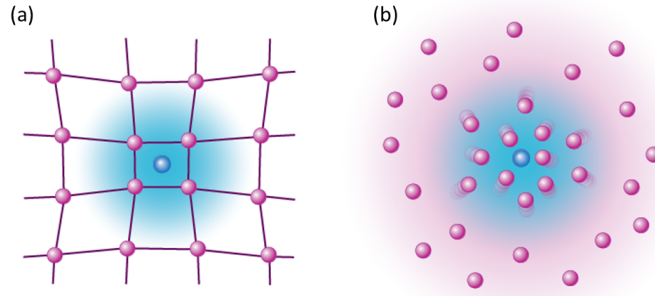
FIGURE 4.1.: (a) Electron in a crystal lattice of atoms. (b) Quantum simulation in which a potassium atom is located in a bath of erbium atoms. Taken from [44].

polaron [22,39]. Although these Bose polarons have already been seen in BECs, our Er-K machine will be novel since the impurities will be located in a dipolar BEC. This allows further tunability of the system due to the dipole-dipole interaction.

4.2.1. Anisotropic Polarons

First, by tilting the dipoles with an external magnetic field away from the axis orthogonal to the panake trap, the dipole-dipole interaction will yield anisotropic phonon modes in the dipolar condensate [40]. These anisotropic phonon modes will dress the impurity atoms and lead to anisotropic polarons [41] which have a differing effective mass along the x and y axes. We will measure the dispersion relation along each axis via momentum-resolved RF spectroscopy [42] to determine the polaron's anisotropicity. First, the impurity potassium atoms are placed in a Zeeman sublevel of the potassium ground state (potentially $|F = 1, m_F = -1\rangle$) which has minimal coupling to the dipolar bath [43]. A RF pulse will then place the atoms into an excited Zeeman sublevel (likely $|F = 1, m_F = 0\rangle$) which strongly interacts with the dipolar bath via s-wave scattering—the scattering length (and therefore the interaction strength) will be tuned via an interspecies Feshbach resonance. After some interaction time t the atoms will be released from the trap and a time-of-flight (TOF) image will be taken. Using an inverse Abel transform, the 3D momentum distribution of the cloud can be determined. By varying the amplitude of the RF pulse and measuring the momentum distribution of the atom cloud each time, the dispersion relation (see Fig. 4.2) can be mapped along all three axes. This will allow us to verify existence of anisotropic polaron modes.
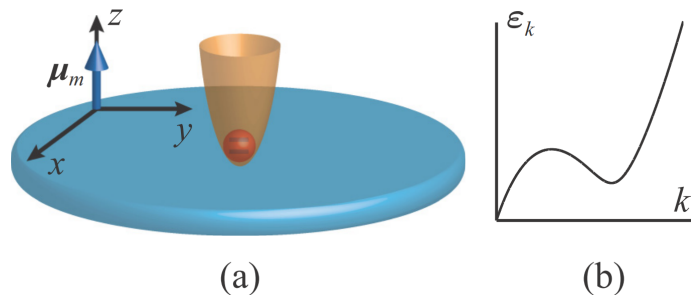
FIGURE 4.2.: (a) Potassium atom in a bath of erbium atoms. The potassium atom is held in a species selective harmonic trap. (b) Roton excitation spectrum can be changed via erbium's dipole-dipole interaction which should allow the non-Markovian dynamics of the system to be tuned. Taken from [24].

4.3. Non-Markovian Reservoirs

Markovian processes are those in which a system loses information to the surrounding environment. In quantum information systems this can be seen when a qubit decoheres due to interactions with environment. However, non-Markovian systems—in which information flows from the environment back to the system—have become highly researched in recent years due to their potential application in quantum metrology [45] and quantum communication [46,46]. One of the proposed experimental systems [47] to study non-Markovianity is a single qubit coupled to a dipolar quantum bath (see Fig. 4.2). This provides a highly tunable environment in which the interactions between the qubit and the bath can be engineered. In particular, theoretical proposals have shown that by increasing the strength of the bath's dipole-dipole interaction the system can be changed from Markovian, to weakly non-Markovian and then to strongly non-Markovian [24]. This is in response to the softening of the bath's excitation spectrum via the roton-mode.

4.4. Decoherence Measurements

Our dual Er-K machine will provide an excellent setup to test these theories by placing potassium impurity atoms in a bath of erbium atoms. We plan to prepare the potassium atoms in one Zeeman sublevel (again $|F = 1, m_F = -1\rangle$) which interacts minimally with the erbium bath. We will use a Ramsey-like inferferometry measurement to determine the decoherence of the system (see Fig. 4.2). This involves using a RF $\pi/2$ pulse to place the atoms in a superposition of the ground state and an excited state (a second Zeeman level $|F = 1, m_F = 0\rangle$, [43]). The
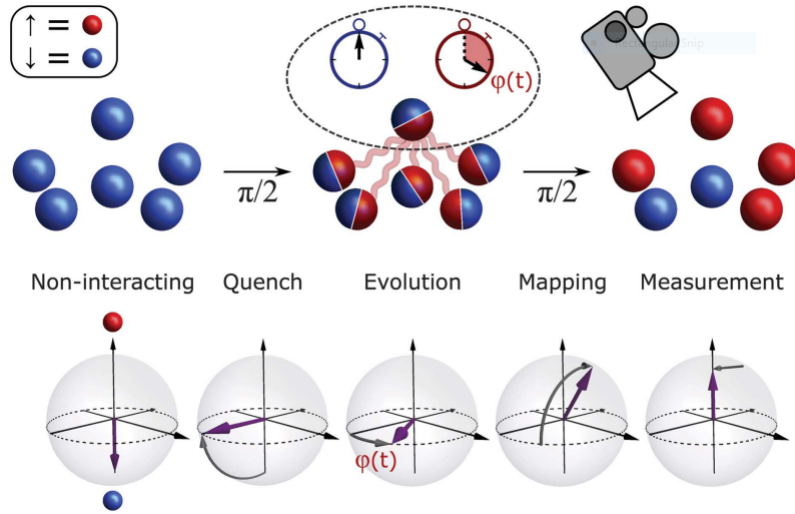
FIGURE 4.3.: (a) Experimental sequence for measuring the impurity decoherence. The atoms are first prepared in a single Zeeman sublevel after which they are placed in a superposition state via a $\pi/2$ pulse and allowed to evolve for time t. A second $\pi/2$ RF pulse with a variable phase is then applied and the Zeeman sublevel populations measured. Taken from [48].

system will then evolve for a time t after which a second RF $\pi/2$ pulse with a variable phase will be applied. Next, the population of the ground and excited Zeeman sublevels will be measured allowing the decoherence to be determined for the given value of t. By repeating the experiment for different values of t the decoherence with respect to time can be measured.

Using a Feshbach resonance, the s-wave scattering length can be changed via magnetic fields. This will allow us to tune the relative strength of the dipole-dipole and contact interactions. As the dipole-dipole interaction becomes stronger than the contact interaction, the system becomes increasingly non-Markovian. Experimentally, this should be seen by revivals of the impurity atom's coherence, rather than the pure exponential decay of the coherence seen in Markovian systems. Additionally, we plan to study the effect of temperature on non-Markovianity by varying the temperature of the bath and performing similar decoherence measurements [25].

Appendices

A. Data Acquisition and Storage Systems

A.1. Introduction

Cicero Word Generator [49] is an experimental control program which was developed in Wolfgang Ketterle's group at MIT by Aviv Keshet to control cold atom experiments and has been adopted to control the erbium experiment. Cicero interacts with the experiment through a secondary program called Atticus server which uses a National Instruments chassis to control both analogue and digital outputs. Unfortunately, at the current time, Cicero is unable to receive inputs and incorporate those into experimental sequences.

A.2. Camera Program

The primary data taken in the experiments are images—namely fluorescence and absorption images. As such, the experiment needed a program to take these images at specified times during the experimental sequence. A Thorlabs camera was purchased and a standalone program written to acquire data from the camera. Since the camera has low-level function written in C++, a Python wrapping script was used. The Python wrapping script was open source and as such had several bugs which needed fixing and more importantly needed extending as not all of the camera's base functions were wrapped.

Although the camera program was written to operate stand-alone, the camera still needed to be able to receive a trigger from Cicero to take an image at the correct time in the experimental sequence. The camera function which takes an image when a trigger is given is blocking which needed to be dealt with by using the timeout function. However, Cicero and the camera control program cannot talk directly to one another and as such a database was used as a go-between. A diagram of this connection can be seen in Fig. A.1

Once the wrapping script was finished a graphical user interface (GUI) was written to allow control of the camera. The GUI allows several camera options to be set
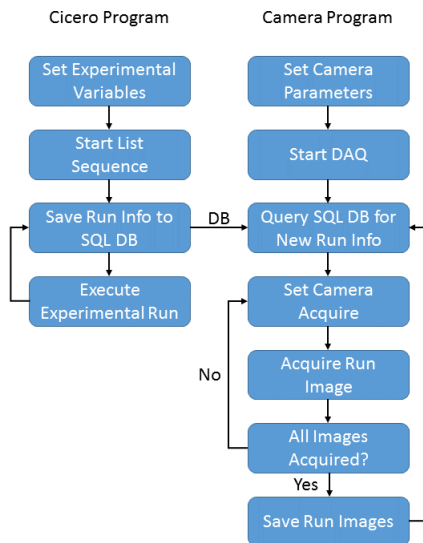
FIGURE A.1.: Programming flow chart for the interaction of the Cicero control program with the camera control program which communicate via the MySQL database.

including the area of interest (AOI), sub-sampling along both the x and y directions as well as other parameters such as gain, exposure time, and black levels. Lastly, all the information pertaining to each image—such as the savepath and the camera settings—are saved to the database for later analysis (see Appendix B).

A.3. MySQL Database

As previously stated, the primary data taken in the experiments are images. However, in addition to this, we need to record the various experimental settings that were used in the production of the image such as current through coils, detunings of lasers and timing of various steps within the experimental sequence. Most of these control parameters are set in Cicero, whereas camera settings are controlled from the stand-alone camera control program. In order to efficiently store data in an organized and relational way, a MySQL database with a normalized data structure (see Fig. A.2) is used. The MariaDB database is currently hosted on the control computer although a separate Linux machine may be purchased in the future to act solely as the database server.

Before every Cicero run starts, the general settings for that run are stored as a row in the runlog table in the database, whereas the Cicero experimental variable values are stored in the sequence variables table. When the camera control program takes
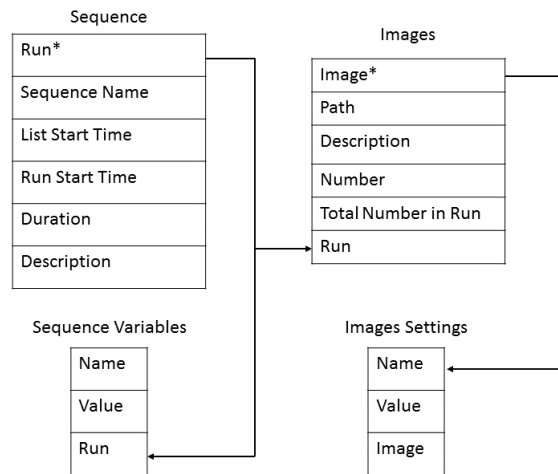
F I G U R E A.2.: Data tables within the MySQL database. Relations between the different tables are denoted with arrows. Stars indicate the key column for the table.

images, it queries the database to determine the last row and thereby the current run. For each image a row is stored in the images table. This includes the path to the image as well as the run the image was taken in. Lastly, a third table is used to store the image settings for each image.

A.4. Storage of Images

During each experimental run a folder is created which stores the Cicero sequence and settings as well as the raw images that were acquired. Since each image has a unique name, the image settings and run information for that image can be easily extracted from the database for analysis. The number of images taken can run into the thousands per day and to minimize the amount of memory used, each image is saved as a compressed .tiff.

B. Data Analysis GUI

B.1. Introduction

Significant amounts of data are generated in physics experiments. The analysis of this data needs to be streamlined and in large part automated for efficiency. In order to organize the data in a coherent way a MySQL database (see Appendix A) was implemented to store experimental data—excepting images which are stored on the file system. Although Python or Matlab scripts can be written to do the data analysis, the programming prowess of the various lab members varies and an analysis GUI (see Fig. B.1) was written to simplify the recall of data from the database. Currently, the GUI is able to pull all the relevant experimental data from both the MySQL database and file system for a given experimental sequence. Additionally, the program automatically renders the raw images into processed images for both fluorescence and absorption sequences. Further analysis tools include the ability to set an area of interest and complete calculations on the data located therein. These calculations include pixel sums, two-dimensional fits and one dimensional summed profiles along both the x and y axes. Of particular interest is the program's ability to automatically detect atom clouds with a specially trained convolutional neural network (CNN).

B.2. Data Retrieval and Raw Image Processing

Although the analysis GUI is the primary way most lab users interact with the data, simple scripts enable more tech savvy users to interact with the data at a higher level. As such, many elements of the data analysis are written such that they can be used in either the GUI or user-made scripts. One of these is the data retrieval Python module (see Fig. B.2). The module allows a folder full of raw images to be imported and correlates the images with the experimental variables from the SQL database that were used to take those images. Furthermore, the database contains information on whether the raw images were part of fluorescence or absorption images and whether the images is an atom, probe or background image. Based on this information an absorption image is calculated with Eq. 2.5 or
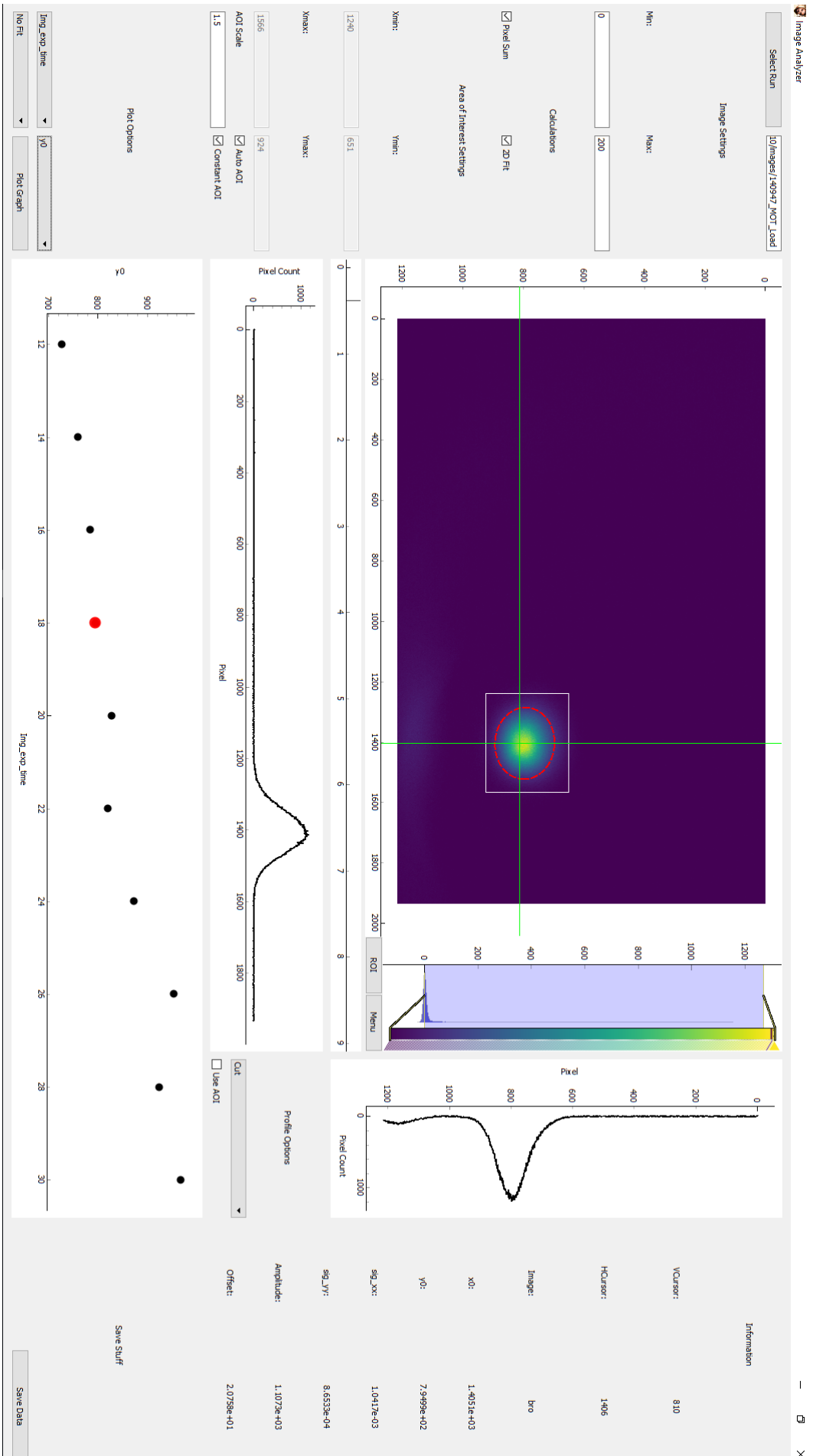
Figure B.1.: The data analysis GUI.

FIGURE B.2.: The data retrieval process.

for fluorescence images the following equation is used

$$I = I_a - I_b \qquad\qquad (\text{B.1})$$

where I_a is the atom intensity and I_b is the background intensity.

B.3. Area of Interest

A single area of interest can be manually set for all the images that are loaded into the GUI or an area of interest can manually be set per image. The area of interest allows further data analysis—such as 2D fitting or pixel sums—only on the portion of the image where the atoms are located. In addition to the ability to manually set the area of interest, the analysis GUI is able to automatically determine where an atomic cloud is located using an object detection neural network (see Appendix C)

B.4. 2D Fitting

Determining the size of the atomic cloud is essential for elucidating information such as the temperature of the atoms. Furthermore, finding the centroid of the atomic cloud's density distribution allows the calibration of lens magnifications. A 2D fit on the atomic cloud allows both of these to be determined. In the previous section we described how the data analysis GUI can provide a subset of the experimental image for further analysis. This is particularly useful for 2D fitting as extraneous data can confuse or create inaccuracies in the fit due to noise or secondary features in the image. Even if the noise is low and only the atomic cloud is present, fitting the entire image is quite computationally intensive and applying the fit to only a small subset of the image can substantially reduce fit times.

B.4.1. GPU Fitting

In an effort to further reduce the fitting times, we implemented a GPU based Python fitting package. This allows us to go from fitting times of approximately 8-12 seconds per image to roughly 1 second. When analysing a run with dozens or even hundreds of images, this can make a significant difference in analysis time.

B.5. 1D Plots

Lastly, a series of 1D plots exist in the data analysis program which allow further information to be ascertained.

B.5.1. Profile Plots

1D plots exists below the main image and to the right of the main image (see Fig. B.1) these allow a 1D profile of the image to be seen along the x and y axes respectively. Options in the GUI allow either a cut-through or a summation to be done over the entire image or only the area of interest. These 1D plots will be particular useful when the experiment reaches quantum degeneracy as the profiles will allow the condensed atoms to be more easily seen on top of the thermal distribution.

B.5.2. Variable Plot

Below the imaging section of the GUI is a 1D plot with two drop down menus next to it. These drop down menus are both populated with a list of variables from the experimental routine (pulled from the MySQL database) and variables from the current analysis, such as a pixel sum within the AOI or the 2D fitting parameters. The variables chosen from each of the boxes are plotted against one another in the 1D plot which is useful when doing scans of a single experimental variable (such as frequency detuning).

C. Object Detection Neural Network

Convolution neural networks have seen a rapid rise in use in the last few years due to their ability to accurately classify images with better than human accuracy. Furthermore, object detection neural networks such as Faster R-CNN [50] and YOLO [51] have the ability to detect the location of an object in the image, classify it and create a bounding box around it. This is of particular relevance in many machine vision applications such as optical communications [52] or detecting atomic clouds.

C.1. Dataset

Deep neural networks rely on large amounts of labelled data during training and validation. This can be problematic in fields where there is a limited amount of existing data or the data has not been labelled. However, in our particular application we can make use of simulated data. Atomic clouds in both 3D MOTs and optical dipole traps can be approximated by a 2D Gaussian and thus we create a set of training data (see Fig. C.1) that is randomized both with respect to the the orientation, radii and centroid location. The bounding box is determined by the $1/e^2$ radius along the x and y axes. Additionally, Gaussian noise is added to the images to approximate noise seen in real environmental conditions with the the mean set to zero (automatic scaling takes care of offsets and differences in amplitude) and the standard deviation randomly chosen. In total we generate 150 images with 100 used for training and 50 used for validation.

C.2. Neural Network and Training

Although several deep learning frameworks exist, we use PyTorch [53] which utilizes a more pure Pythonic approach than Tensorflow. Additionally, rather than writing a custom neural network, we use a Faster R-CNN [50] with a ResNet50 [54] backbone and simply change the number of classes it can detect i.e. the number
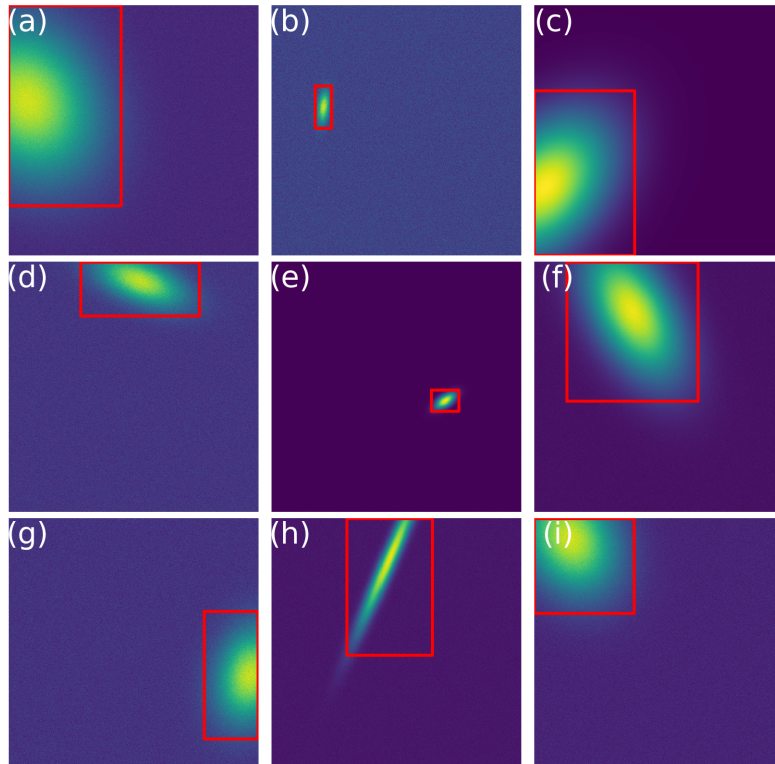
FIGURE C.1.: Example of random elliptical Gaussians used to train the object-detection neural network. The areas of interest coincides with the $1/\mathrm{e}^2$ radius along the x and y axes and are denoted by the red squares.

of final outputs. Additionally, we use a neural network pre-trained on the COCO dataset which decreases the amount of time required for training and also increases the accuracy of the final network [55]. Since training is significantly speeded up using parallel processing chips such as graphical processing chips (GPU) or tensor processing chips (TPU) we write our code in a Google Colab notebook and then train in the cloud with Google's free GPU resources.

Our neural network thus has two classes, one for the atomic cloud and one for the background. We use stochastic gradient descent as the optimizer with the learning rate initially set to 0.005, the momentum $=0.09$ and a batch size of two. A learning rate scheduler is also implemented which decreases the learning rate by an order of magnitude every three epochs. These hyperparameters were sufficient to train our NN to a high degree of accuracy; however, should a more complex dataset be utilized and the pre-set hyperparameters not achieve similar accuracy, Bayesian optimization could be use for hyperparameter tuning with either the Ax package from Facebook or SciKit Optimize. Finally, we train our neural network for ten epochs.

C.3. Experimental Data

Although the neural network (NN) is both trained and validated on the simulated data, it must ultimately work on experimental images (see Fig C.2). Thus, we implemented the NN in both our data analysis scripts and our data analysis GUI. In almost every case where we can detect an atomic cloud by eye, the neural network accurately detects the AOI of the cloud. One fringe case where the neural network struggles slightly is when the peak intensity of the cloud becomes comparable with the peak noise on the image (e.g. at the end of a time of flight sequence). However, this is most likely because the training data didn't have such high relative noise values. In the future this can be addressed by augmenting the training data.
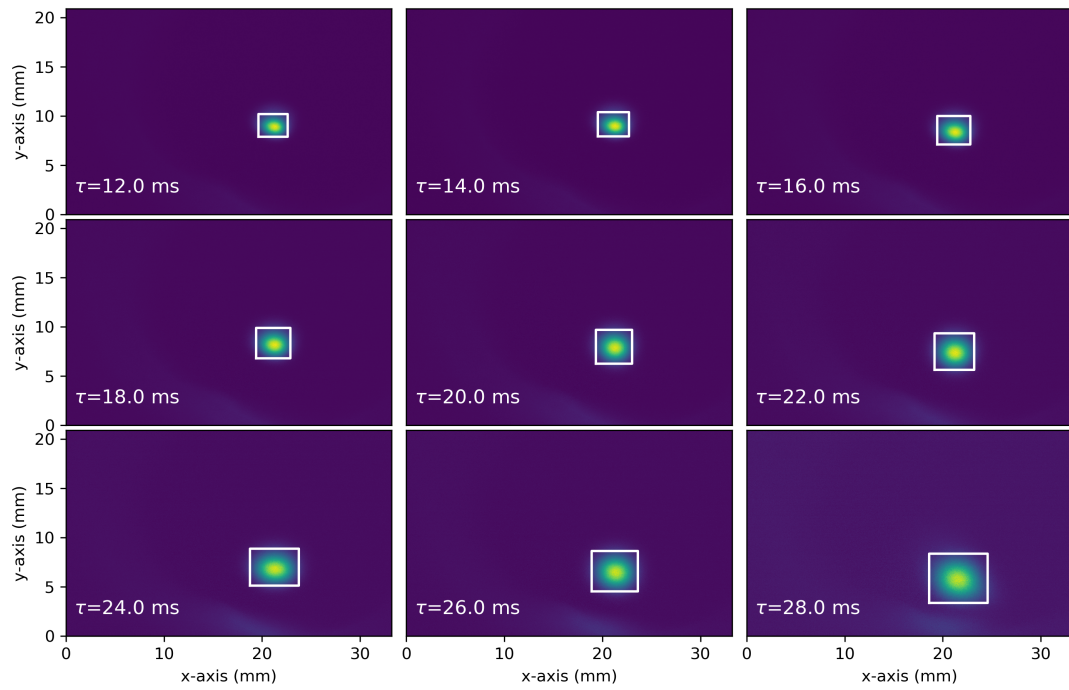
Figure C.2.: Time of flight data in which an atomic cloud is released from a compressed MOT. The time after release is given by τ (ms) and the object detection neural atomic determines the area of interest (red box) for later data analysis.

Bibliography

[1] M. H. Anderson, J. R. Ensher, M. R. Matthews, C. E. Wieman, E. A. Cornell, *et al.*, "Observation of Bose-Einstein condensation in a dilute atomic vapor," *Science*, vol. 269, no. 5221, pp. 198–201, 1995.

[2] K. B. Davis, M.-O. Mewes, M. R. Andrews, N. Van Druten, D. Durfee, D. Kurn, and W. Ketterle, "Bose-Einstein condensation in a gas of sodium atoms," *Physical Review Letters*, vol. 75, no. 22, p. 3969, 1995.

[3] A. Griesmaier, J. Werner, S. Hensler, J. Stuhler, and T. Pfau, "Bose-Einstein condensation of chromium," *Physical Review Letters*, vol. 94, no. 16, p. 160401, 2005.

[4] M. Lu, N. Q. Burdick, S. H. Youn, and B. L. Lev, "Strongly dipolar Bose-Einstein condensate of dysprosium," *Physical Review Letters*, vol. 107, no. 19, p. 190401, 2011.

[5] K. Aikawa, A. Frisch, M. Mark, S. Baier, A. Rietzler, R. Grimm, and F. Ferlaino, "Bose-Einstein condensation of erbium," *Physical Review Letters*, vol. 108, no. 21, p. 210401, 2012.

[6] T. Lahaye, J. Metz, B. Froehlich, T. Koch, M. Meister, A. Griesmaier, T. Pfau, H. Saito, Y. Kawaguchi, and M. Ueda, "d-wave collapse and explosion of a dipolar Bose-Einstein condensate," *Physical Review Letters*, vol. 101, no. 8, p. 080401, 2008.

[7] L. Chomaz, R. M. van Bijnen, D. Petter, G. Faraoni, S. Baier, J. H. Becher, M. J. Mark, F. Waechtler, L. Santos, and F. Ferlaino, "Observation of roton mode population in a dipolar quantum gas," *Nature Physics*, vol. 14, no. 5, p. 442, 2018.

[8] D. Petter, G. Natale, R. van Bijnen, A. Patscheider, M. Mark, L. Chomaz, and F. Ferlaino, "Probing the roton excitation spectrum of a stable dipolar Bose gas," *Physical Review Letters*, vol. 122, no. 18, p. 183401, 2019.

[9] S. Giovanazzi and D. H. O'Dell, "Instabilities and the roton spectrum of a quasi-1D Bose-Einstein condensed gas with dipole-dipole interactions," *The European Physical Journal D-Atomic, Molecular, Optical and Plasma Physics*, vol. 31, no. 2, pp. 439–445, 2004.

[10] L. Santos, G. Shlyapnikov, and M. Lewenstein, "Roton-maxon spectrum and stability of trapped dipolar Bose-Einstein condensates," *Physical Review Letters*, vol. 90, no. 25, p. 250403, 2003.

[11] L. Chomaz, D. Petter, P. Ilzhöfer, G. Natale, A. Trautmann, C. Politi, G. Durastante, R. van Bijnen, A. Patscheider, M. Sohmen, *et al.*, "Long-lived and transient supersolid behaviors in dipolar quantum gases," *Physical Review X*, vol. 9, no. 2, p. 021012, 2019.

[12] G. Natale, R. van Bijnen, A. Patscheider, D. Petter, M. Mark, L. Chomaz, and F. Ferlaino, "Excitation spectrum of a trapped dipolar supersolid and its experimental evidence," *Physical Review Letters*, vol. 123, no. 5, p. 050402, 2019.

[13] F. Böttcher, J.-N. Schmidt, M. Wenzel, J. Hertkorn, M. Guo, T. Langen, and T. Pfau, "Transient supersolid properties in an array of dipolar quantum droplets," *Physical Review X*, vol. 9, no. 1, p. 011051, 2019.

[14] M. Guo, F. Böttcher, J. Hertkorn, J.-N. Schmidt, M. Wenzel, H. P. Büchler, T. Langen, and T. Pfau, "The low-energy goldstone mode in a trapped dipolar supersolid," *Physical Review X*, vol. 9, no. 1, pp. 386–389, 2019.

[15] I. Ferrier-Barbut, H. Kadau, M. Schmitt, M. Wenzel, and T. Pfau, "Observation of quantum droplets in a strongly dipolar Bose gas," *Physical Review Letters*, vol. 116, no. 21, p. 215301, 2016.

[16] M. Schmitt, M. Wenzel, F. Böttcher, I. Ferrier-Barbut, and T. Pfau, "Self-bound droplets of a dilute magnetic quantum liquid," *Nature*, vol. 539, no. 7628, p. 259, 2016.

[17] L. Chomaz, S. Baier, D. Petter, M. Mark, F. Wächtler, L. Santos, and F. Ferlaino, "Quantum-fluctuation-driven crossover from a dilute Bose-Einstein condensate to a macrodroplet in a dipolar quantum fluid," *Physical Review X*, vol. 6, no. 4, p. 041039, 2016.

[18] F. Wächtler and L. Santos, "Quantum filaments in dipolar Bose-Einstein condensates," *Physical Review A*, vol. 93, no. 6, p. 061603, 2016.

[19] A. L. Gaunt, T. F. Schmidutz, I. Gotlibovych, R. P. Smith, and Z. Hadzibabic, "Bose-Einstein condensation of atoms in a uniform potential," *Physical Review Letters*, vol. 110, no. 20, p. 200406, 2013.

[20] A. L. Gaunt and Z. Hadzibabic, "Robust digital holography for ultracold atom trapping," *Scientific reports*, vol. 2, p. 721, 2012.

[21] N. Navon, A. L. Gaunt, R. P. Smith, and Z. Hadzibabic, "Critical dynamics of spontaneous symmetry breaking in a homogeneous bose gas," *Science*, vol. 347, no. 6218, pp. 167–170, 2015.

[22] N. B. Jørgensen, L. Wacker, K. T. Skalmstang, M. M. Parish, J. Levinsen, R. S. Christensen, G. M. Bruun, and J. J. Arlt, "Observation of attractive and repulsive polarons in a Bose-Einstein condensate," *Physical Review Letters*, vol. 117, no. 5, p. 055302, 2016.

[23] J. Wang, X.-J. Liu, and H. Hu, "Roton-induced Bose polaron in the presence of synthetic spin-orbit coupling," *Physical Review Letters*, vol. 123, no. 21, p. 213401, 2019.

[24] J.-B. Yuan, H.-J. Xing, L.-M. Kuang, and S. Yi, "Quantum non-Markovian reservoirs of atomic condensates engineered via dipolar interactions," *Physical Review A*, vol. 95, no. 3, p. 033610, 2017.

[25] S.-Q. Tang, J.-B. Yuan, X.-W. Wang, and D.-Y. Zhang, "Temperature can enhance Non-Markovianity in dipolar Bose–Einstein condensate," *Journal of Low Temperature Physics*, vol. 189, no. 3-4, pp. 147–157, 2017.

[26] J. J. McClelland and J. L. Hanssen, "Laser cooling without repumping: a magneto-optical trap for erbium atoms," *Physical Review Letters*, vol. 96, no. 14, p. 143005, 2006.

[27] M. Krstajic, "Erbium BEC in an optical box potential." 2018.

[28] A. Frisch, *Dipolar Quantum Gases of Erbium.* PhD thesis, University of Innsbruck, 2014.

[29] G. Salomon, L. Fouché, S. Lepoutre, A. Aspect, and T. Bourdel, "All-optical cooling of k 39 to Bose-Einstein condensation," *Physical Review A*, vol. 90, no. 3, p. 033405, 2014.

[30] H.-Z. Chen, X.-C. Yao, Y.-P. Wu, X.-P. Liu, X.-Q. Wang, Y.-X. Wang, Y.-A. Chen, and J.-W. Pan, "Production of large K 41 Bose-Einstein condensates using d 1 gray molasses," *Physical Review A*, vol. 94, no. 3, p. 033408, 2016.

[31] D. Dreon, L. A. Sidorenkov, C. Bouazza, W. Maineult, J. Dalibard, and S. Nascimbene, "Optical cooling and trapping of highly magnetic atoms: the benefits of a spontaneous spin polarization," *Journal of Physics B: Atomic, Molecular and Optical Physics*, vol. 50, no. 6, p. 065005, 2017.

[32] J. Sanz. Personal Communication.

[33] C. R. Cabrera Córdova, "Quantum liquid droplets in a mixture of Bose-Einstein condensates," 2018.

[34] T. Tiecke, "Properties of potassium," *University of Amsterdam, The Netherlands, Thesis*, pp. 12–14, 2010.

[35] C. R. C. Cordova, *Quantum liquid droplets in a mixture of Bose-Einstein condensates*. PhD thesis, Universitat Politècnica de Catalunya, 2018.

[36] M. Sbroscia, *Between order and disorder: ultracold atoms in a quasicrystalline optical lattice*. PhD thesis, University of Cambridge, 2019.

[37] C. Ravensbergen, V. Corre, E. Soave, M. Kreyer, E. Kirilov, and R. Grimm, "Production of a degenerate Fermi-Fermi mixture of dysprosium and potassium atoms," *Physical Review A*, vol. 98, no. 6, p. 063624, 2018.

[38] H. Fröhlich, H. Pelzer, and S. Zienau, "Xx. properties of slow electrons in polar materials," *The London, Edinburgh, and Dublin Philosophical Magazine and Journal of Science*, vol. 41, no. 314, pp. 221–242, 1950.

[39] M.-G. Hu, M. J. Van de Graaff, D. Kedar, J. P. Corson, E. A. Cornell, and D. S. Jin, "Bose polarons in the strongly interacting regime," *Physical Review Letters*, vol. 117, no. 5, p. 055301, 2016.

[40] G. Bismut, B. Laburthe-Tolra, E. Maréchal, P. Pedri, O. Gorceix, and L. Vernac, "Anisotropic excitation spectrum of a dipolar quantum bose gas," *Physical Review Letters*, vol. 109, oct 2012.

[41] B. Kain and H. Y. Ling, "Polarons in a dipolar condensate," *Physical Review A*, vol. 89, p. 023612, feb 2014.

[42] J. T. Stewart, J. P. Gaebler, and D. S. Jin, "Using photoemission spectroscopy to probe a strongly interacting fermi gas," *Nature*, vol. 454, pp. 744–747, aug 2008.

[43] M. G. Skou, T. G. Skov, N. B. Jørgensen, K. K. Nielsen, A. Camacho-Guardian, T. Pohl, G. M. Bruun, and J. J. Arlt, "Non-equilibrium dynamics of quantum impurities," *arXiv preprint arXiv:2005.00424*, 2020.

[44] F. Chevy, "Viewpoint: Bose polarons that strongly interact," Jul 2016.

[45] A. W. Chin, S. F. Huelga, and M. B. Plenio, "Quantum metrology in non-Markovian environments," *Physical Review Letters*, vol. 109, no. 23, p. 233601, 2012.

[46] R. Vasile, S. Olivares, M. A. Paris, and S. Maniscalco, "Continuous-variable quantum key distribution in non-Markovian channels," *Physical Review A*, vol. 83, no. 4, p. 042321, 2011.

[47] H. Shen, S. Xu, S. Yi, and X. Yi, "Controllable dissipation of a qubit coupled to an engineering reservoir," *Physical Review A*, vol. 98, no. 6, p. 062106, 2018.

[48] R. J. Fletcher, R. Lopes, J. Man, N. Navon, R. P. Smith, M. W. Zwierlein, and Z. Hadzibabic, "Two-and three-body contacts in the unitary bose gas," *Science*, vol. 355, no. 6323, pp. 377–380, 2017.

[49] A. Keshet and W. Ketterle, "A distributed, graphical user interface based, computer control system for atomic physics experiments," *Review of Scientific Instruments*, vol. 84, no. 1, p. 015105, 2013.

[50] S. Ren, K. He, R. Girshick, and J. Sun, "Faster r-cnn: Towards real-time object detection with region proposal networks," in *Advances in neural information processing systems*, pp. 91–99, 2015.

[51] J. Redmon and A. Farhadi, "Yolov3: An incremental improvement," *arXiv preprint arXiv:1804.02767*, 2018.

[52] L. Hofer, L. Jones, J. Goedert, and R. Dragone, "Hermite–Gaussian mode detection via convolution neural networks," *JOSA A*, vol. 36, no. 6, pp. 936–943, 2019.

[53] A. Paszke, S. Gross, S. Chintala, G. Chanan, E. Yang, Z. DeVito, Z. Lin, A. Desmaison, L. Antiga, and A. Lerer, "Automatic differentiation in pytorch," 2017.

[54] K. He, X. Zhang, S. Ren, and J. Sun, "Deep residual learning for image recognition," in *Proceedings of the IEEE conference on computer vision and pattern recognition*, pp. 770–778, 2016.

[55] J. Yosinski, J. Clune, Y. Bengio, and H. Lipson, "How transferable are features in deep neural networks?," in *Advances in neural information processing systems*, pp. 3320–3328, 2014.